Journal of Materials Chemistry C

MnFe0.5Ru0.5O3: An Above-Room-Temperature Antiferromagnetic Semiconductor

Journal:	*Journal of Materials Chemistry C*
Manuscript ID	TC-ART-10-2018-005059.R1
Article Type:	Paper
Date Submitted by the Author:	08-Nov-2018

Complete List of Authors:	Tan, Xiaoyan; George Mason University, Chemistry & Biochemistry McCabe, Emma; University of Kent, School of Physical Sciences Orlandi, Fabio; ISIS Pulsed Neutron and Muon Source, Manuel, Pascal; Rutherford Appleton Laboratory, ISIS Facility Batuk, Maria; University of Antwerp, Physics Hadermann, Joke; University of Antwerp, Deng, Zheng; Institute of physics, Chinese Academy of Sciences Jin, Changqing; Institute of Physics Chinese Academy of Sciences Nowik, Israel; The Hebrew University of Jerusalem, Racah Institute of Physics Herber, Rolfe; The Hebrew University of Jerusalem, Racah Institute of Physics Segre, Carlo; Illinois Institute of Technology, Physics & CSRRI Liu, Sizhan; New Jersey Institute of Technology, Department of Physics Croft, Mark ; Rutgers, The State University of New Jersey Kang, Chang-Jong; Rutgers The State University of New Jersey Lapidus, Saul H. ; Argonne National Laboratory, X-ray Science Division, Argonne, Illinois 60439, United States, X-ray Science Division Frank , Corey ; Rutgers The State University of New Jersey, Chemistry & Chemical Biology Padmanabhan , Haricharan ; Pennsylvania State University, Department of Materials Science and Engineering Gopalan , Venkatraman ; Pennsylvania State University, Department of Materials Science and Engineering Wu, Meixia ; School of Chemistry, Sun Yat-Sen University Li, Man-Rong; Sun Yat-Sen University, School of Chemistry ; Rutgers, The State University of New Jersey, Chemistry and Chemical Biology Greenblatt, Martha; Rutgers The State University of New Jersey, Chemistry & Chemical Biology Kotliar, Gabriel; Rutgers, The State University of New Jersey Walker, David; Lamont-Doherty Earth Observatory

$MnFe_{0.5}Ru_{0.5}O_3$: An Above-Room-Temperature Antiferromagnetic Semiconductor

Xiaoyan Tan,[1,†] Emma E. McCabe,[2] Fabio Orlandi,[3] Pascal Manuel,[3] Maria Batuk,[4] Joke Hadermann,[4] Zheng Deng,[5] Changqing Jin,[5] Israel Nowik,[6] Rolfe Herber,[6] Carlo U. Segre,[7] Sizhan Liu,[8] Mark Croft,[9] Chang-Jong Kang,[9] Saul Lapidus,[10] Corey E. Frank,[1] Haricharan Padmanabhan,[11] Venkatraman Gopalan,[11] Meixia Wu,[12] Man-Rong Li,[12] Gabriel Kotliar,[9] David Walker,[13] Martha Greenblatt*,[1]

[1]Department of Chemistry and Chemical Biology Rutgers, The State University of New Jersey, Piscataway, New Jersey, 08854, United States.
[2]School of Physical Sciences, University of Kent, Canterbury, Kent, CT2 7NH, United Kingdom.
[3]ISIS Facility, STFC, Rutherford Appleton Laboratory, Chilton, Didcot, Oxfordshire, OX11 0QX, United Kingdom.
[4]EMAT, University of Antwerp, Groenenborgerlaan 171, B-2020 Antwerp, Belgium.
[5]Institute of Physics, School of Physics, University of Chinese Sciences, P. O. Box 603, Beijing, 100190, P. R. China.
[6]Racah Institute of Physics, the Hebrew University, Jerusalem, 91904, Israel.
[7]Department of Physics & CSRRI, Illinois Institute of Technology, Chicago, Illinois, 60616, United States.
[8]Department of Physics, New Jersey Institute of Technology, Newark, New Jersey, 07102, United States.
[9]Department of Physics and Astronomy, Rutgers, The State University of New Jersey, Piscataway, New Jersey, 08854, United States
[10]Advanced Photon Source, Argonne National Laboratory, Argonne, Illinois, 60439, United States
[11]Department of Materials Science and Engineering, Pennsylvania State University, University Park, Pennsylvania 16802, United States
[12]Key Laboratory of Bioinorganic and Synthetic Chemistry of Ministry of Education, School of Chemistry, Sun Yat-Sen University, Guangzhou, 510275, P. R. China
[13]Lamont Doherty Earth Observatory, Columbia University, Palisades, New York, 10964, United States
*Corresponding author's e-mail: greenbla@chem.rutgers.edu

Abstract

A transition-metal-only $MnFe_{0.5}Ru_{0.5}O_3$ polycrystalline oxide was prepared by a reaction of starting materials MnO, MnO_2, Fe_2O_3, RuO_2 at 6 GPa and 1873 K for 30 minutes. A combination of X-ray and neutron powder diffraction refinements indicated that $MnFe_{0.5}Ru_{0.5}O_3$ adopts the corundum (a-Fe_2O_3) structure type with space group $R\bar{3}c$, in which all metal ions are disordered. The centrosymmetric nature of the $MnFe_{0.5}Ru_{0.5}O_3$ structure is corroborated by transmission electron microscopy, lack of optical second harmonic generation, X-ray absorption near edge spectroscopy, and Mössbauer spectroscopy. X-ray absorption near edge spectroscopy of $MnFe_{0.5}Ru_{0.5}O_3$ showed the oxidation states of Mn, Fe, and Ru to be 2+/3+, 3+, and ~4+, respectively. Resistivity measurements revealed that $MnFe_{0.5}Ru_{0.5}O_3$ is a semiconductor. Magnetic measurements and magnetic structure refinements indicated that $MnFe_{0.5}Ru_{0.5}O_3$ orders antiferromagnetically around 400 K, with magnetic moments slightly canted away from the c axis. ^{57}Fe Mössbauer confirmed the magnetic ordering and Fe^{3+} ($S = 5/2$) magnetic hyperfine splitting. First principles calculations are provided to understand the electronic structure more thoroughly. A comparison of synthesis and properties of $MnFe_{0.5}Ru_{0.5}O_3$ and related corundum $Mn_2BB'O_6$ derivatives is discussed.

Introduction

Spintronics (spin-based electronics or spin transport electronics) is an emergent new technology that takes advantage of the interaction between the charge and magnetic spins of the electrons in materials. Compared to conventional semiconductor charge-based electronics, devices based on spintronics consume less electric power, provide faster data processing speed and increased storage densities.[1, 2] Promising spintronic materials are ferromagnetic/ferrimagnetic semiconductors (FMS/FiMS) due to the possibility of spin-polarized carriers and facile combination with semiconductor devices.[1] For practical application, the ideal FMS/FiMS should exhibit magnetic ordering above room temperature (RT). Designing and finding such materials is still challenging for scientists in materials science, solid state chemistry, condensed matter physics, and related areas.[3] To date, there are few FMS/FiMS materials with an ordering temperature near or above RT such as spinel $Fe_{0.5}Cu_{0.5}Cr_2S_4$ (T_C = 340 K),[4] perovskite $Sr_{0.8}Y_{0.2}CoO_{3-\delta}$ (T_C = 335 K, 310 K for thin films),[5, 6] and double perovskites (DP) La_2NiMnO_6 (T_C ~ 280 K) and Sr_2CrOsO_6 (T_C ~ 700 K).[7-9]

Compared to ferromagnets, antiferromagnets are more common in nature. Recent studies indicate that antiferromagnetic semiconductors (AFMS) could be alternatives to FMS in spintronics, which motivates further research into the AFM spintronics subfield.[10-20] Several near/above RT candidates have been discovered including LiMnAs (T_N = 374 K),[21] CuMnAs (T_N = 295 K),[22, 23] FeRh (T_N ~ 373 K),[24] MnTe (T_N = 310 K),[25] and perovskite-type Sr_2IrO_4 (T_N = 240 K).[26, 27] However, further development of the AFM spintronics subfield requires the discovery of more AFMS with T_N above RT.

As mentioned above, DPs are promising spintronic materials with high magnetic ordering temperatures. In particular, DP and corundum related oxides, $A_2BB'O_6$, have demonstrated the required properties. Besides La_2NiMnO_6 (T_C ~ 280 K) and Sr_2CrOsO_6 (T_C ~ 700 K),[7-9] we recently synthesized several $Mn_2^{2+}Fe^{3+}B'^{5+}O_6$ (B' = Nb, Ta, Mo, Re) phases under high pressure and temperature, where both the A and B sites are transition metals.[28-30] High pressure synthesis of Mn_2FeNbO_6 and Mn_2FeTaO_6 at 1573 K under 7 GPa produced $LiNbO_3$ (LN)-type polar AFM insulators with weak FM magnetic ordering around 210 K.[28] The magnetic interactions of Mn^{2+} (high spin (HS), d^5) and Fe^{3+} (HS, d^5) ions (alongside diamagnetic Nb^{5+} and Ta^{5+} ions) are responsible for magnetic transition temperatures close to RT. The magnetic transition temperature of $Mn_2FeB'O_6$ are further increased by incorporating more d^n ($n > 0$) electrons at the B' sites. When Nb^{5+} (d^0) is replaced by Mo^{5+} (d^1), the polar Ni_3TeO_6 (NTO)-type $Mn^{2+}Fe^{3+}Mo^{5+}O_6$ obtained under 8 GPa is an FiMS with T_C = 337 K.[29] In the case of B'^{5+} = Re^{5+}(d^2), the DP $Mn^{2+}Fe^{3+}Re^{5+}O_6$ formed at 5 GPa displays giant magnetoresistance as a half-metallic ferrimagnet with T_C = 520 K.[30] Following this trend, it was expected that Nb^{5+} (d^0) could also be substituted by Ru^{5+}(d^3) in $MnFe_{0.5}Ru_{0.5}O_3$ for possible magnetic ordering above RT.

Here, we report that $MnFe_{0.5}Ru_{0.5}O_3$ can be synthesized under high pressure and high temperature. The crystal structure, formal oxidation states of cations, magnetic and electrical properties have been investigated. Neutron diffraction and Mössbauer spectroscopy data were also measured to elucidate the magnetic ordering in the structure. First principles calculations were undertaken to understand the electronic structure more thoroughly. Good agreement is found between the experiments and the DFT calculations.

Experimental Section

Starting Materials and Synthesis. Polycrystalline $MnFe_{0.5}Ru_{0.5}O_3$ was prepared by high-pressure and high-temperature synthesis with a Walker-type Multi-Anvil press as described in our previous work.[28-31] A stoichiometric mixture of MnO (wt. 99.99%, Alfa Aesar), MnO_2 (wt. 99.996%, Alfa Aesar), Fe_2O_3 (wt. 99.999%, Sigma Aldrich) and RuO_2 (wt. 99.9%, Alfa Aesar) was first ground well at ambient pressure. The oxide mixture was then packed into a Pt capsule inside a MgO crucible, which was later assembled with other parts of the high-pressure apparatus. The reaction was carried out at 1873 K under 6 GPa for 0.5 h and then quenched to room temperature in a few minutes. After quenching, the pressure was slowly released. The resulting sample was a black pellet, with a total mass of ~25 mg. To make enough sample (~100 mg) for neutron experiment, four experiments were carried out with the same synthetic conditions, and the resulting samples were checked by X-ray powder diffraction (XRPD).

Chemical Analysis. The chemical composition of the samples was determined by energy dispersive X-ray (EDX) analysis conducted on a JEOL 5510 scanning electron microscope equipped with an INCAx-sight 6587 system (Oxford Instruments). Mn-K, Fe-K and Ru-L lines were used for the composition quantification.

Thermogravimetric Analysis (TGA) and Differential Scanning Calorimetry (DSC). A powder sample of about 30 mg was loaded into an alumina crucible and measured in an SDT Q600 TA Instrument. The sample was tested from room temperature to 1000 °C at a heating and cooling rate of 10 °C/min under Ar flow. The remaining powder after the measurement was analyzed by XRPD.

X-ray Powder Diffraction (XRPD). Samples were measured in the 2θ range from 10° to 80° and collected for 1 h on a Bruker D8 Advance Diffractometer (Cu Kα, λ =1.5418 Å) with a SOL-X solid state detector. RT synchrotron powder X-ray diffraction (λ = 0.4126 Å) was collected in the 2θ range from 0.5° to 50° at the 11-BM beam line at the Advanced Photon Source (APS) of Argonne National Laboratory. High-resolution powder X-ray diffraction data were also collected at room temperature on a Rigaku SmartLab X-ray diffractometer using a Ge220 monochromator to select the Cu Kα, λ =1.5418 Å wavelength.

Neutron Powder Diffraction (NPD). NPD data were collected on ~100 mg $MnFe_{0.5}Ru_{0.5}O_3$ powder sample placed inside a 3 mm diameter thin-walled cylindrical vanadium can at the ISIS neutron and muon source (Rutherford Appleton Laboratory, U.K.) on the WISH diffractometer located in the second target station.[32] Multibank (153°, 122°, 90°, 58°, 27°) data were collected at 450 K (~30 minutes) and the sample was then cooled to 5 K in a closed-cycle refrigerator (CCR) and a high quality dataset (~2 hours) was recorded. Shorter scans were then collected on warming (~ 15 minutes scans in 20 K increments to 75 K, and then at 25 K increments to 300 K, with longer 60 minutes scans collected at 60 and 125 K). Rietveld refinements were carried out with Topas Academic[33, 34] and the magnetic symmetry analysis was carried out with ISODISTORT.[35]

Transmission Electron Microscopy (TEM). The samples for TEM analysis were prepared by mixing the powders with ethanol in an ultrasonic bath and depositing a few drops of the obtained suspension onto a holey TEM grid covered with carbon. Electron diffraction (ED) patterns were acquired with a Phillips

CM20 microscope operated at 200 kV. High angle annular dark field (HAADF) scanning transmission electron microscopy (STEM) images were acquired with a FEI Titan 80-300 "cubed" microscope operated at 300 kV. The simulated HAADF-STEM images were calculated with the QSTEM software.[36]

Second Harmonic Generation (SHG). The measurements were done in far-field reflection geometry at normal incidence inside a cryostat. A pulsed laser beam from a Ti:sapphire femtosecond laser with a wavelength of 800 nm (pulse width 80 fs, repetition rate 80 MHz) was focused on a polished polycrystalline pellet sample with a 50x objective onto a spot size of 0.5 μm. The reflected light was passed through a filter to eliminate the 800 nm fundamental, and then collected with a photomultiplier tube to detect any signal at the second harmonic of 400 nm.

X-ray Absorption Near Edge Spectroscopy (XANES). XANES was carried out to confirm the formal oxidation state of the cations in $MnFe_{0.5}Ru_{0.5}O_3$. Mn, Fe and Ru K-edge data were collected at the 10-ID and 11-ID beam line at the APS of Argonne National Laboratory and the 8-ID ISS beamline at the National Synchrotron Light Source II (NSLS-II), at Brookhaven National Laboratory. The Ru L2,3-edge measurements were performed at the NSLS-II TES, 8-BM beamline. Standard spectra collected previously at X19A at (NSLS-I) are also included over most of the energy ranges.

Magnetic Measurements. Magnetic properties were measured on polycrystalline sample with a Quantum Design SQUID MPMS-XL magnetometer. Field-cooled (FC) and zero-field-cooled (ZFC) magnetizations were measured between 1.8 and 300 K in a direct-current applied field. Field dependence of isothermal magnetization was measured with the applied field varying from -6 to 6 T.

Mössbauer Spectroscopy. The ^{57}Fe Mössbauer studies were performed with a conventional constant acceleration drive in transmission mode, in conjunction with a 50 mCi ^{57}Co:Rh source. The absorber, $MnFe_{0.5}Ru_{0.5}O_3$, was crushed to fine powder and put into a Perspex absorber holder. Measurements were performed while the absorber was in a cryostat with temperature stabilization (to 0.5°) in the range of 90 to 400 K. The obtained spectra were analyzed, in terms of a least square fit procedure, to simulated model spectra.

Electrical Resistivity. Resistivity measurements were conducted with a Quantum Design Physical Property Measurement System (PPMS) with standard four-probe technique.

DFT calculations. Density functional theory (DFT) was used to investigate the type of crystal structure and magnetic order that give stable phases, to confirm the experimental findings. To treat the structural disorder observed in the experiments, the virtual crystal approximation (VCA) method[37] implemented in Quantum Espresso code[38, 39] was employed within the Vanderbilt ultra-soft-pseudopotential scheme.[40] The kinetic energy cutoffs for wave functions and charge density were set to be 50 and 400 Ry, respectively in the VCA calculations. After the stable crystal structure was found through the VCA calculations, the electronic structures have been studied with two different magnetic structures (antiferro- and ferro-magnetic ordering) using the full-potential linearized augmented plane-wave method implemented in WIEN2k.[41] In the magnetic calculations, the structural disorder was ignored and the Fe occupancy was regarded to be 100 % at the disordered sites for simplicity. Generalized gradient approximation (GGA) of

Perdew-Burke-Ernzerhof (PBE)[42] was used for the exchange-correlation functional and 25 × 25 × 7 *k* points were used for the Brillouin zone sampling. To obtain the correct ground state (including the magnetic moment of Fe^{3+} and an insulating phase), GGA+U was adopted within fully localized limit.[43, 44] The effective on-site Coulomb interaction parameter U_{eff} = U – J = 4 eV was used.

Results and Discussion

Crystal Structure and Thermal Stability. Similar to the synthesis of Mn_2FeMO_6 (*M*= Nb, Ta, Mo, W, Re), $MnFe_{0.5}Ru_{0.5}O_3$ was prepared at 1873 K under 6 GPa with a Walker-type Multi-Anvil press. Incident illumination, plane-polarized optical micrographs shows the target phase with ~100 μm grain size, and trace of RuO_2 and $FeMnO_x$ impurities (Figure. S2). The XRPD pattern (Figure. S2) indicates either a disordered α-Fe_2O_3-type (Figure 1a, corundum, $R\bar{3}c$) or LN-type (Figure 1b, $R3c$) as the main phase with a small amount RuO_2 impurity (~ wt. 2%). Both structures give the same allowed reflections in diffraction experiments due to Friedel's law.

Both corundum and LN crystal structures have the same 3-dimensional (3D) construction based on distorted MO_6 (*M* = Mn, Fe, or Ru) octahedra. The centrosymmetric corundum crystal structure consists of symmetric dimers of MO_6 octahedra connected via face-sharing along the [001] direction and edge-sharing in (001) planes. All metal sites are disordered, and each MO_6 (*M* = Mn/Fe/Ru) is distorted with *M* cations displaced from the centers of octahedra, resulting in three long and three short M-O bond distances (Figure 1a). The cation-ordered non-centrosymmetric LN structure is derived from this corundum structure, but with two cation sites, allowing ordering of Mn, Fe and Ru over these sites (e.g. a Mn site, and a mixed Fe/Ru site). This would give a LN model with distorted dimers of MnO_6 and MO_6 (*M* = Fe, Ru) octahedra face-sharing along [001] (Figure 1b). Besides LN, other corundum derivatives are centrosymmetric ilmenite (IL, $R\bar{3}$), noncentrosymmetric ordered ilmenite (OIL, *R*3), and NTO (*R*3), which have the same 3D network of MO_6 octahedra but with different cation arrangements.[45]

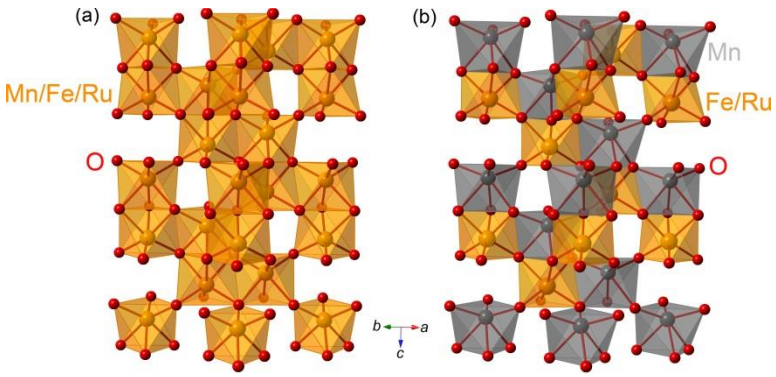

Figure 1. Crystal structures of $MnFe_{0.5}Ru_{0.5}O_3$ with α-Fe_2O_3 type (a, corundum, $R\bar{3}c$), and LN-type (b, $R3c$) viewed along the [110] direction. Color code: $(Mn/Fe/Ru)O_6$ = orange in (a), MnO_6/$(Fe/Ru)O_6$ = gray/orange in (b), O = red spheres.

The chemical composition of $MnFe_{0.5}Ru_{0.5}O_3$ was confirmed by EDX with the formula $Mn_{2.01(8)}Fe_{1.00(6)}Ru_{1.00(12)}O_x$ and the thermal stability of this sample was measured by TGA-DSC. Above 800°C, the sample starts decomposing into $MnFe_2O_4$, or $FeMn_2O_4$ and RuO_2 (Figure S3).

X-ray and Neutron Powder Diffraction. Because Rietveld refinements with XRPD data gave similar fits to corundum ($R\bar{3}c$) or LN-type ($R3c$) structure (Figure. S2), and Fe and Mn are indistinguishable to Cu Kα radiation, RT XRPD data were used to determine only the distribution of Ru over the two cation sites in the LN model. Refinements suggested a statistical distribution of Ru over the two sites, with Ru occupancies of 0.27(2) at (0 0 z), and 0.23(2) at (0 0 0), respectively. The R_{wp} from this model is 7.12%, which is slightly smaller than that (7.15%) of a disordered LN model with Ru occupancies of 0.25 on both sites (Figure S4, Table S1-2) analogous to the corundum model due to cation disorder. Therefore, a statistical distribution of Ru seems most likely in $MnFe_{0.5}Ru_{0.5}O_3$ based on XRPD data analysis.

The Ru distribution was then fixed (Ru occupancies of 0.25 on both sites) in a starting LN model for multibank refinement using 450 K NPD data to refine the distribution of Fe and Mn over the two sites. NPD is expected to be very sensitive to this distribution, given the strong contrast in neutron scattering lengths (Mn = -3.73 fm, Fe = 9.54 fm, Ru = 7.21 fm).[46] A fully disordered LN model (analogous to corundum) gave a good fit to the data (R_{wp} = 3.192%). Allowing the Fe and Mn distribution to refine resulted in a marginal improvement in fit (R_{wp} = 3.179%) but suggested an almost statistical distribution of Fe and Mn over the two sites, Ru/Fe/Mn occupancy of 0.25/0.227(3)/0.523(3) at (0 0 z), and 0.25/0.275(3)/0.477(3) at (0 0 0) (Figure S5, Table S3). This analysis suggests that a fully disordered corundum model is most appropriate to describe the crystal structure of $MnFe_{0.5}Ru_{0.5}O_3$, at least at the length scale probed by diffraction techniques.

The disordered corundum model was then used for multibank (153°, 122°, 90°, 58°, 27° banks of data) Rietveld refinement of 450 K NPD data, and the results are shown in Figure 2 (122° bank data fit profile), Tables 1-2, and Figure S6 (all bank data fit profiles). Several small impurity phases were also included in the refinements, including RuO_2 (wt. 3.2(1)%), $FeMn_2O_4$ (wt. 2.1(1)%) and Mn_3O_4 (wt. 4(1)%).

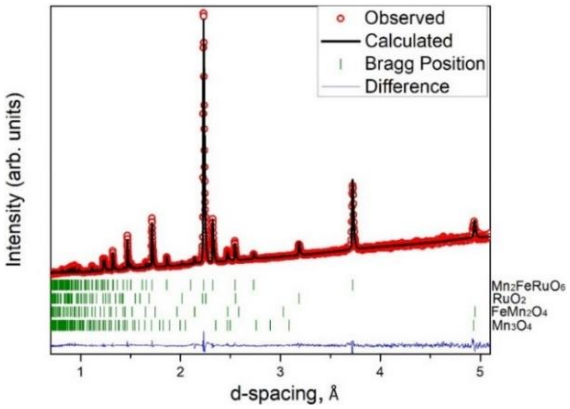

Figure 2. Refinement profiles for $MnFe_{0.5}Ru_{0.5}O_3$ in corundum ($R\bar{3}c$) model, using 450 K NPD 122° bank data. Observed, calculated, Bragg position, and difference profiles are shown in red, black, green, and blue, respectively.

Table 1. Refinement details of corundum ($R\bar{3}c$) model of $MnFe_{0.5}Ru_{0.5}O_3$ using 450 K NPD data with a = 5.0870(1) Å, c = 13.9306(3) Å; R_{wp} = 3.19%, R_p = 3.04% and χ^2 = 2.27.

Atom	site	x	y	z	Factional occupancy	U_{iso} × 100 (Å^2)
Mn/Ru/Fe	12c	0	0	0.3497(1)	0.5/0.25/0.25	2.55(9)

O	18*e*	0.3073(1)	0	0.25	1	2.54(7)

Table 2. Selected bond lengths and angles from Rietveld refinement of corundum ($R\bar{3}c$) model of $MnFe_{0.5}Ru_{0.5}O_3$ using 450 K NPD data.

Bond	Length (Å)	Angle	(°)
M – O	3 × 1.997(1)	*M* – O(1) – *M* (within open face)	99.93(5)
M – O	3 × 2.090(1)	*M* – O(1) – *M* (from open to shared face)	91.01(1)
M – *M*	1 × 2.777(3)	*M* – O(1) – *M* (within shared face)	80.71(5)

The refined unit cell parameters are a = 5.0870 (1) Å, c = 13.9306(3) Å, V = 360.5(8) Å^3 (Table 1). The unit cell parameter a of $MnFe_{0.5}Ru_{0.5}O_3$ is much smaller than those of LN-type Mn_2FeMO_6 (M = Nb, Ta, a ~ 5.27 Å), while the *c-axis* is slightly larger than that of Mn_2FeTaO_6 (c = 13.8892(3) Å), but smaller than that of Mn_2FeNbO_6 (c = 13.9338(2) Å). The average *M*-O bond lengths are about 2.05 Å (Table 2), which is much shorter than those of Mn-O in $Mn^{2+}{}_2Fe^{3+}NbO_6$ (2.16 Å) and $Mn^{2+}{}_2Fe^{3+}TaO_6$ (2.22 Å). These values are also smaller than those (~ 2.2 Å) in other corundum derivative analogs such as $Mn^{2+}{}_2Fe^{3+}M^{5+}O_6$ (M = Mo, Sb) and $Mn^{2+}{}_2Fe^{2+}W^{6+}O_6$. The *M*-O bond length analysis indicates that Mn is likely not purely Mn^{2+} in the structure. The average *M*-O bond length (~2.05 Å) is comparable with those in $Mn^{2+}{}_2Fe^{3+}Nb^{5+}O_6$ (2.035 Å), $Mn^{2+}{}_2Fe^{3+}Ta^{5+}O_6$ (2.01 Å), $Mn^{2+}{}_2Fe^{3+}Mo^{5+}O_6$ (2.033 Å), and $Mn^{2+}{}_2Fe^{3+}Sb^{5+}O_6$ (2.006 Å). However, they are shorter than those in $Mn^{2+}{}_2Fe^{2+}W^{6+}O_6$ (2.154 Å), which support Fe^{3+} in $MnFe_{0.5}Ru_{0.5}O_3$. The detailed cation oxidation states will be discussed in the XANES results.

Transmission Electron Microscopy. To distinguish between LN-type *R*3*c* and corundum $R\bar{3}c$ models for $MnFe_{0.5}Ru_{0.5}O_3$, as shown in Figure 1, TEM experiments were also carried out. Electron diffraction patterns of $MnFe_{0.5}Ru_{0.5}O_3$ are shown in Figure 3 and S7, respectively. The patterns agree with the reflection conditions of the *R*3*c* and $R\bar{3}c$ space groups: *hkl*: $-h + k + l = 3n$; *hk*0: $-h + k = 3n$; $h\bar{h}l$: $h + l = 3n$, $l = 2n$; *hhl*: $l = 3n$; 00*l*: $l = 6n$. In Figure S6, reflection $0\bar{1}1$ and its symmetrically equivalent reflections in the [211] zone and 00*l*: $l = 3n$ in the [210] zone are due to double diffraction. Based only on selected area ED patterns, it is impossible to distinguish between *R*3*c* and $R\bar{3}c$ space groups. Therefore, we tested the models for the two space groups against experimental HAADF-STEM images.

In the LN *R*3*c* models, there are distinct columns of *A* and *B*/*B*′ sites of different stoichiometry, while in the corundum $R\bar{3}c$ model, all three atomic species are intermixed. There are two projections that allow separate visualization of the *A* and *B*/*B*′ columns in the *R*3*c* structure: [100] and [$2\bar{2}1$]. On HAADF-STEM images, the brightness of the dots is proportional to the average atomic number of the projected column: $I \sim Z^2$. In $MnFe_{0.5}Ru_{0.5}O_3$, Z_{Mn} = 25, Z_{Fe} = 26, Z_{Ru} = 44 and therefore in case of ordering, columns with on average heavier cations should appear brighter.

HAADF-STEM images were taken along both those [100] and [$2\bar{2}1$] directions (Figure 3c, d). There is no systematic difference in the intensity of the different atomic columns. The ratio between the summed intensity of *A* and *B*/*B*′ sites, from profiles of 10 different rows of either *A* or *B*/*B*′, is very close to 1. Moreover, intensity profiles for ten rows with pairs of *A* and *B*/*B*′ columns (Figure S8) do not show any systematic difference in the intensities. The differences between the *A* and *B*/*B*′ peaks are random and can be explained by a statistical difference in the occupation of one column to the next. Therefore, there is no ordering between Mn, Fe and Ru cations in $MnFe_{0.5}Ru_{0.5}O_3$ and the results agree with an $R\bar{3}c$ (and not an

*R*3*c*) model, which is consistent with the results from XRPD and NPD analysis above, and with the disorder suggested by SHG, XANES and Mössbauer data below.

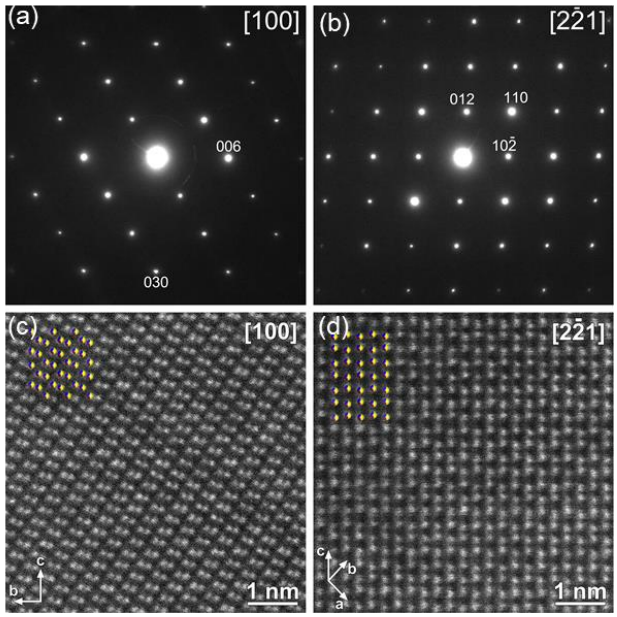

Figure 3. Electron diffraction patterns (a, b) and HAADF-STEM images (c, d) of $MnFe_{0.5}Ru_{0.5}O_3$ along [100] and [2$\bar{2}$1] directions.

Second Harmonic Generation. SHG is a sensitive probe of inversion symmetry breaking in single crystal and polycrystalline materials. The SHG response of polycrystalline $MnFe_{0.5}Ru_{0.5}O_3$ was probed with SHG microscopy. Similar techniques have been used by the authors in the past to study inversion symmetry breaking in single crystal and polycrystalline complex oxides.[47] Measurements were carried out at 300 and 25 K. There is no SHG signal above the background noise level at either temperature, which indicates that the material is centrosymmetric in this temperature range.

X-ray Absorption Near Edge Spectroscopy. XANES measurements were performed to probe the Mn, Fe, Ru oxidation state in $MnFe_{0.5}Ru_{0.5}O_3$. The Fe-K main-edge in $MnFe_{0.5}Ru_{0.5}O_3$ appears to correspond to ~Fe^{3+} with somewhat broad main edge features bearing some similarity to the LN structure standard spectra for Mn_2FeMO_6 (*M* = Ta and Nb) (Figure 4).

Interestingly, compared to Mn_2FeMO_6 spectra, the $MnFe_{0.5}Ru_{0.5}O_3$ spectrum manifests two features, an additional shoulder on the initial rising portion of the main edge (labeled "1" in Figure 4a), and a prominent absolute-peak shifted to higher energy (labeled "2" in Figure 4a). These two features are however present (albeit being more sharply defined) in the corundum (α-Fe_2O_3) standard spectrum. Thus, the Fe-K main-edge appears to support a corundum (α-Fe_2O_3) structure for $MnFe_{0.5}Ru_{0.5}O_3$.

The Mn-K main-edge in $MnFe_{0.5}Ru_{0.5}O_3$ is dramatically different from those of the LN structure standard spectra for Mn_2FeMO_6 (*M* = Ta and Nb) (Figure 5), thereby precluding a ~Mn^{2+}, LN structure in this compound. In terms of chemical shift, the Mn-K main edge appears to be consistent with a substantial

$Mn^{\sim 3+}$ component, which is similar to that of its Fe-K edge in Figure 4a. A comparison of the near-edge and post-edge fine structure features (Figure S9) emphasize the similar features over the entire energy range, which suggests that the Mn and Fe sites in $MnFe_{0.5}Ru_{0.5}O_3$ are the same and are essentially the same as that in the corundum α-Fe_2O_3 compound. The notably larger shoulder (on the leading main-edge rise), and decreased intensity in the peak-region of spectrum (relative to the shifted Fe spectrum) indicates a greater admixture of Mn^{2+} character at the Mn sites.

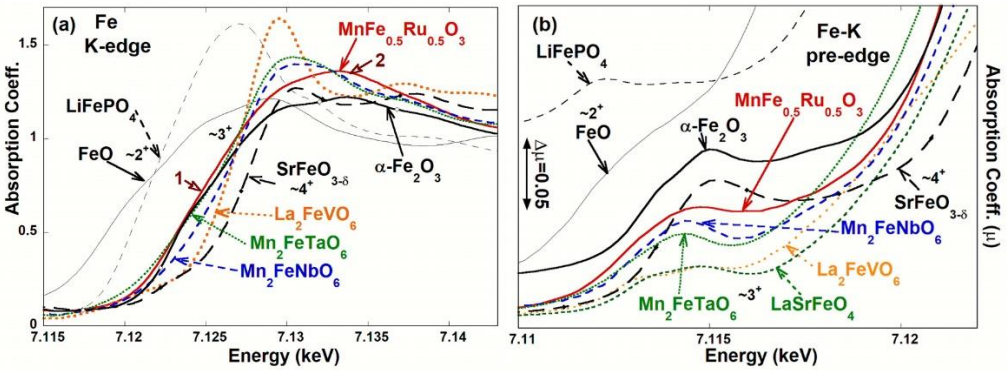

Figure 4. The Fe-K main-edge (a) and pre-edge (b) spectra for $MnFe_{0.5}Ru_{0.5}O_3$ and other Fe compounds with varying formal valences: the ~2+ standards FeO and $LiFePO_4$; the ~3+ perovskite standard La_2FeVO_6, the ~3+ corundum α-Fe_2O_3, and the ~3+ $LiNbO_3$–type standards Mn_2FeMO_6 (M = Ta and Nb); and the ~4+ standard $SrFeO_3$, all of which have octahedral Fe-O coordination.

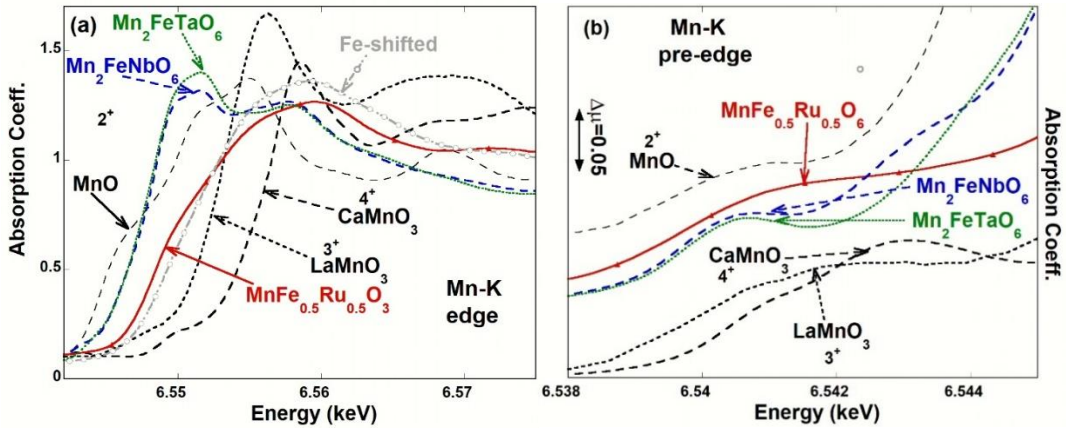

Figure 5. The Mn-K main edge (a) and pre-edge spectra (b) for $MnFe_{0.5}Ru_{0.5}O_3$ and other Mn compounds with varying formal valences: the ~2+ standards MnO, the LN structure Mn_2FeMO_6 (M = Ta and Nb) standards; the perovskite based ~3+ $LaMnO_3$; and ~4+ $CaMnO_3$ standards. Note the Fe-shifted curve in which the Fe-K edge for the compound (from Figure 4a) has been shifted down energy by 0.57397 keV, the difference in the peak energies of MnO and FeO.

The Mn-K pre-edge of $MnFe_{0.5}Ru_{0.5}O_3$ is substantially broadened compared to the pre-edges of the LN structure standards (Figure 5b). Moreover, the pre-edges of the LN structures standards are significantly different from the $MnFe_{0.5}Ru_{0.5}O_3$ pre-edge, yet again arguing for a corundum structure and against a LN structure.

Based on the chemical shift of the Ru-K edge as compared with Ru and RuO_2 standards (Figure 6a), the Ru valence state is close-to, or somewhat-less-than the Ru^{4+} state in RuO_2. The $L_{2,3}$-edges of 4*d* transition metals are sensitive to the electron configuration both through the chemical shift and the structure of the intense near edge "white line" (WL) features.[48-54] The chemical shift of the Ru-$L_{2,3}$ edge spectra in $MnFe_{0.5}Ru_{0.5}O_3$, compared to the Sr_2YRuO_6 (Ru^{5+}, d^3), and Y_2CoRuO_6 (Ru^{4+}, d^4) standards (Figure 6b), are clearly consistent with a ~d^4 Ru^{+4} configuration. The intense WL-features at the $L_{2,3}$ edges of 4*d* transition metal sites in compounds with octahedral O-ligand coordination manifest a distinctly bimodal A/B feature structure due to transitions into empty t_{2g}/e_g d-states. The filling of the t_{2g}-states with increasing d-electron count is reflected in the $L_{2,3}$ edge spectra by a systematic decrease in the A-feature intensity (relative to the B-feature) as illustrated in Figure S10 for L_3 edge spectra for a series of d^0 to d^4 compounds.

In Figure 6b, the dramatic decrease in relative A-feature intensity between the Sr_2YRuO_6 (Ru^{5+}, d^3) and Y_2CoRuO_6 (Ru^{4+}, d^4) standards should be noted. For the $MnFe_{0.5}Ru_{0.5}O_3$ $L_{2,3}$ edge spectra, the A-feature intensity appears as an unresolved shoulder on the B-feature. In view of the multiple local environments in the Mn/Fe/Ru site distribution, the inhomogeneity broadening of the ligand field splitting (and the A/B-feature) is reasonable. The amplitude of the A-feature is consistent with a ~d^4 Ru^{4+} configuration. Therefore, both the spectral chemical shift and WLA/B-feature are suggestive of a somewhat reduced Ru^{4+} valence. These observations are consistent with the Fe^{3+} and mixed $Mn^{2+/3+}$ suggested by XANES results.

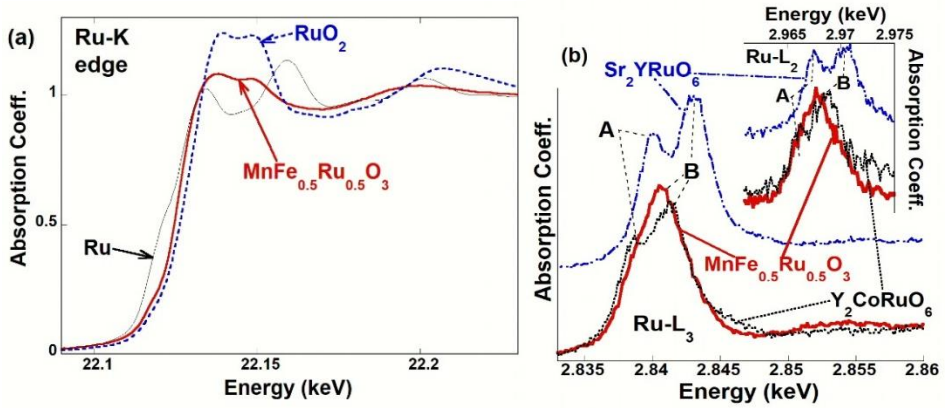

Figure 6. (a) A comparison of the Ru-K edge spectra for $MnFe_{0.5}Ru_{0.5}O_3$ to the Ru and RuO_2 standards. (b) A comparison of the Ru-L_3 edge spectra for $MnFe_{0.5}Ru_{0.5}O_3$ to the Sr_2YRuO_6 and Y_2CoRuO_6 standards (lower left) along with the Ru-L_2 edge spectra for the same compounds (inset upper right). Note the A- and B-features related respectively to transitions into empty t_{2g} and e_g final states.

Magnetic Properties. FC and ZFC magnetic susceptibilities of polycrystalline samples indicate a transition around 375 K (Figure 7). As the temperature decreases, the FC magnetic susceptibility keeps increasing, and two slight transitions occur near 80 and 45 K, respectively. These two transitions are more obvious when the sample is measured with lower magnetic field (Figure S11). The observed divergence between ZFC-FC curves is due to the anisotropy in the sample, which decreases as the magnetic field increases (Figure S11).

Based on the above NPD analysis, the sample contains a small amount of $FeMn_2O_4$ (T_C = 373, 50 K),[55] and Mn_3O_4 (T_N = 42 K) [56] impurities. Temperature dependent NPD (Figure 9) indicates that the sample orders AFM around 400 K. There are no additional magnetic transitions; no additional reflections or changes in the temperature behavior of the magnetic Bragg peaks were observed below 80 K, Figure S12. Therefore, the high transition temperature near 375 K may stem from both the sample and possible impurity $FeMn_2O_4$ or isostructural $Fe_{1+x}Mn_{2-x}O_4$ ($0 < x < 1$). The small low temperature transitions can be attributed to impurities $Fe_{1+x}Mn_{2-x}O_4$ and Mn_3O_4. The above RT magnetic transition feature is reminiscent of those of Mn_2FeMoO_6 (T_C =337 K),[29] and Mn_2FeReO_6 (T_C = 520 K).[30]

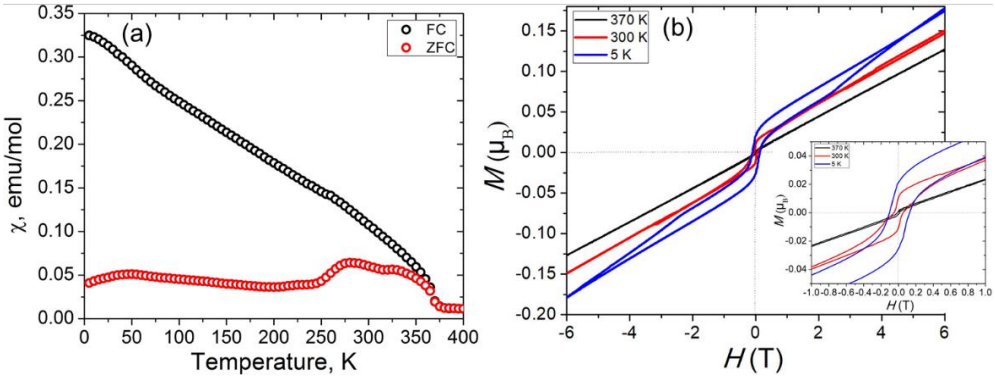

Figure 7. (a) FC and ZFC magnetic susceptibilities of $MnFe_{0.5}Ru_{0.5}O_3$ as a function of temperature with the applied magnetic field of 0.1 T. (b) Isothermal magnetization as a function of field measured at 5, 300, 370 K. Inset in (b) shows the magnetization between -1 and 1 T.

The isothermal magnetization measured at 370 K (Figure 7b) shows almost linear behavior above 50 Oe, and there is almost no hysteresis at this temperature. However, the magnetization measured at 300 and 5 K increased more abruptly at low field (below 2000 Oe) and hysteresis loops were observed at both temperatures. As the temperature decreases, the hysteresis loops enlarge, with larger remnant magnetization and coercivity (Figure S13). The overall maximum moment at 6 T is very small, which confirms the AFM ordering and possible FiM ordering from impurity $Fe_xMn_{3-x}O_4$.

Magnetic Structure. To understand the nature of the magnetic ordering, neutron diffraction data were recorded from 5 to 450 K. Compared to the data collected at 450 K, additional magnetic Bragg reflections 021 at ~2.2 Å, 101 at ~4.2 Å, and 003 at ~3.6 Å were observed in NPD data collected at 5 K (Figure 8, S12). These were indexed by a magnetic unit cell with the same dimensions as the nuclear unit cell. Magnetic intensity is observed for 00*l* reflections, indicating a significant component of the moments within the *ab* plane.

ISODISTORT[35] was used to explore possible magnetic structures (Table S6), and those with $m\Gamma_3$ modes predicted some intensity in the positions of the magnetic Bragg reflections. The data is best fit with the cation disordered ($R\bar{3}c$) nuclear structure and a $P\bar{1}$ magnetic unit cell (Figure S14, $a_{mag} = b_{mag}\ a_n$; $c_{mag} \approx$ 5.48 Å; $\alpha_{mag} = \beta_{mag} \approx 62.4°$; $\gamma_{mag} = 60°$) with magnetic moments in-plane described $m\Gamma_{3+}$ modes, and an additional out-of-plane (AFM) component described by a $m\Gamma_{1+}$ mode. This low symmetry magnetic model

allows four independent in-plane magnetic $m\Gamma_{3+}$ modes that are highly correlated in analysis using powder diffraction data, since powder data are not sensitive to the in-plane spin direction.

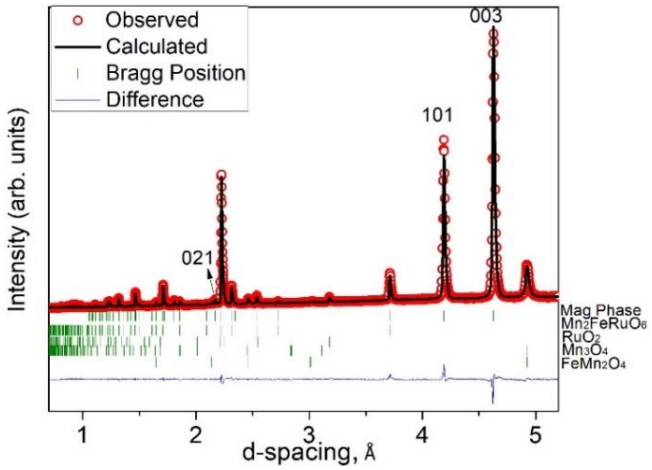

Figure 8. NPD refinement profiles for $MnFe_{0.5}Ru_{0.5}O_3$ in corundum ($R\bar{3}c$) model at 5 K (122° bank data). Observed, calculated and difference profiles are shown in red, black and blue, respectively. Green ticks show reflection positions for the magnetic ordering in $MnFe_{0.5}Ru_{0.5}O_3$, RuO_2, Mn_3O_4, and $FeMn_2O_4$ Pawley phase in order.

The best fit was obtained with $P\bar{1}$ magnetic model, with two in-plane $m\Gamma_{3+}$ modes (with constraints to give modes of opposite sign) and one mode ($m\Gamma_{3+}$ E* 2(a)) constrained to be $1/\sqrt{3}$ in magnitude smaller than the other ($m\Gamma_{3+}$ E* 1(a)). This gives a collinear AFM magnetic model with moments antiparallel and oriented along [120]. This constrained model gives an equivalent fit to the unconstrained model ($\boldsymbol{R}_{wp}$ values for the two models are identical to two decimal places), and gives equal moments on each site as expected for this cation-disordered semiconducting oxide (and avoids high levels of correlation for the unconstrained models). The fit is improved noticeably (R_{wp} decreased by ~1%) if the out-of-plane (AFM) $m\Gamma_{1+}$ mode is also included, allowing the moments to cant out of the *ab* plane. The combination of in-plane AFM $m\Gamma_{3+}$ modes (Figure S15a) and an out-of-plane AFM $m\Gamma_{1+}$ mode (Figure S15b) give the resulting AFM structure (Figure 9a).

The components of the moments along the $P\bar{1}$ magnetic unit cell are $a = \pm 1.256(5)\ \mu_B$, $b = \pm 1.256\ (5)\ \mu_B$, $c = \pm 1.59(1)\ \mu_B$. This is equivalent to components along Cartesian axes of $\mu_x = \pm 2.618(5)\ \mu_B$, $\mu_y = \pm 1.512(3)\ \mu_B$, $\mu_z = \pm 1.340(8)\ \mu_B$, giving overall an in-plane moment $\mu_{xy} = 3.023(6)\ \mu_B$ and an overall moment of $3.307(7)\ \mu_B$ per site at 5 K. The resulting ordered moment (3.3 μ_B at 5 K) in $MnFe_{0.5}Ru_{0.5}O_3$ is very close to that expected for a mixed $Mn^{2+}/Mn^{3+}/Fe^{3+}/Ru^{4+}$ site (3.28 μ_B). We note that this combination of the two AFM irreducible representations (irreps) Γ_{3+} and Γ_{1+} also allows the Γ_{2+} irrep, which describes a FM component along [001]. Although analysis of our diffraction data does not indicate the presence of this out-of-plane FM component, we cannot exclude its presence as a secondary order parameter. However, we note that the hysteresis loop measured for $MnFe_{0.5}Ru_{0.5}O_3$ (Figure 7b) suggests that any such component must be very small. Details from the multibank refinement at 5 K are given in Table S4, 5 and refinement profiles are shown in Figure 8, S16.

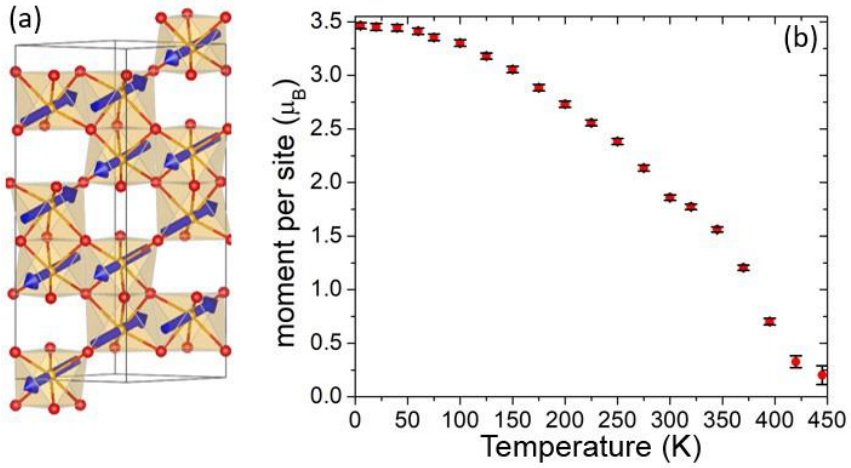

Figure 9. (a) Magnetic structure of $MnFe_{0.5}Ru_{0.5}O_3$ at 5 K (Color code: Mn/Fe/Ru = orange, O = red, magnetic moment = blue arrow). (b) Refined magnetic moment per site as a function of temperature.

The collinear AFM magnetic structure described here for $MnFe_{0.5}Ru_{0.5}O_3$ (Figure 9) is similar to the collinear FiM structure reported for Mn_2FeSbO_6 (IL-type, $R\bar{3}$) at 150 K, in which Mn and Fe sublattices are coupled AFM in the *ab* plane.[57] The absence of FiM in corundum $MnFe_{0.5}Ru_{0.5}O_3$ is due to cation disorder and the absence of two AF-coupled sublattices. AFM interactions also exist in related NTO-type (*R*3) materials such as Ni_3TeO_6, Mn_2FeWO_6, Mn_2FeMoO_6 and Mn_2MnWO_6, which show more complicated magnetic structures as a result of three ordered metal sites leading to competition between the different magnetic sublattices.[29, 58-60] Ni_3TeO_6 exhibits a collinear AFM structure with all Ni moments along the *c* axis with FM honeycomb planes.[58, 59] The magnetic structure of Mn_2FeWO_6 is a collinear spin arrangement with Mn2 spins antiparallel to both Mn1 and Fe spins. In Mn_2FeMoO_6, a more complicated FiM is revealed with all spins parallel to the *c* axis but antiparallel between sub-lattices Fe, Mn1, and Mo, Mn2.[29] Mn_2MnWO_6, however, adopts a non-collinear AFM magnetic structure due to frustration.[60] The canting of spins arrangement in $MnFe_{0.5}Ru_{0.5}O_3$ is also observed in the double perovskite Mn_2FeReO_6, where an AFM Mn lattice and a FiM Fe and Re lattice are canted away from the *c* axis.[30]

The magnetic ordering temperature of $MnFe_{0.5}Ru_{0.5}O_3$ is tracked by the intensity of the magnetic-only reflections 021, 101 and 003, which smoothly decreases (Figure S12) as the temperature is warmed up from 5 to 445 K. Magnetic Bragg reflections are clearly observed in data collected at 395 K, but are absent at 420 K, which indicates that the transition temperature of the sample is around 400 K. Sequential refinements were then carried out with the 122° bank data which show that the moment per cation site decreases smoothly from 3.46(2) μ_B per site at 5 K to 0.70(3) μ_B per site at 395 K (Figure 9b). The refined magnetic moments are close to zero at 425 and 445 K, at which no magnetic Bragg reflections are observed (Fig. S12a). The slight change of slope in parameters derived from sequential Rietveld refinements (magnetic moment as a function of temperature, Figure 9b; relative intensities of magnetic-only reflections, Figure S12) reflects the change in heating sequence and sample environment: NPD data were first collected on heating the sample from 300 K to 450 K in vacuum before the sample was cooled down to 2 K, with 150mBar at RT of He as exchange gas, and further data collected on heating back up to 300 K.

Mössbauer Spectroscopy. The experimental Mössbauer spectra of the $MnFe_{0.5}Ru_{0.5}O_3$ absorber, show that at 97 K all Fe ions are equivalent, since all are in magnetic saturation (Figure 10). The high field in saturation (490 KGauss) proves that the Fe ions are all trivalent (S = 5/2), which is in agreement with XANES results. The low temperature spectra (T < 250 K) were fitted with absorption lines of Lorentzian lineshape, the absorption lines are slightly broadened as the temperature increases.

However, when the temperature is raised to above 250 K, the absorption line widths start to broaden to a large extent, as in the spectrum at 300 K (Figure 10), and are most evident at 350 K (Figure S17). The 373 K spectrum contains a mixture of a sharp paramagnetic quadrupole doublet and a smeared magnetic subspectrum, which indicates that the magnetic phase transition is not sharp (Figure 10). At 386 K, an almost pure quadrupole doublet with a tiny magnetic field (4 KGauss) is still present. These results indicate that the Fe sublattice is already paramagnetic above T_C (Fe) = 390 K, consistent with the appearance of magnetic Bragg peaks in NPD data collected below 395 K.

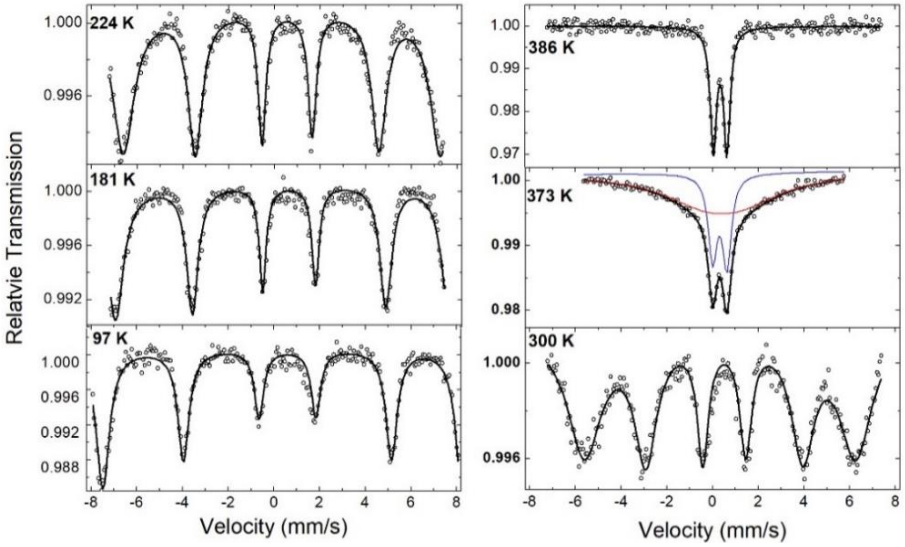

Figure 10. The $MnFe_{0.5}Ru_{0.5}O_3$ Mössbauer spectra at various temperatures.

The spectra at 300 and 350 K require the presence of large hyperfine field distribution, indicating that the Fe ions are not all equivalent magnetically, and the spectra resemble the features of a spin glass structure, or spin fluctuation rates in the magnetic hyperfine splitting window. The temperature dependence of the average hyperfine field (HF) is displayed in Figure 11, in terms of HF (T/T_C)/ HF(0), where T_C = 390 K and HF (0) = 490 KGauss. The fact that the temperature dependence of the experimental magnetic hyperfine field is quite different from a pure magnetic Fe^{3+} sublattice, indicates that Fe ions interact also with the Mn sublattice and possibly also with the magnetic Ru, present also in the Fe sublattice. The broadening phenomena in the Mössbauer spectra strongly support the disordered model of Fe/Mn/Ru in corundum $MnFe_{0.5}Ru_{0.5}O_3$.

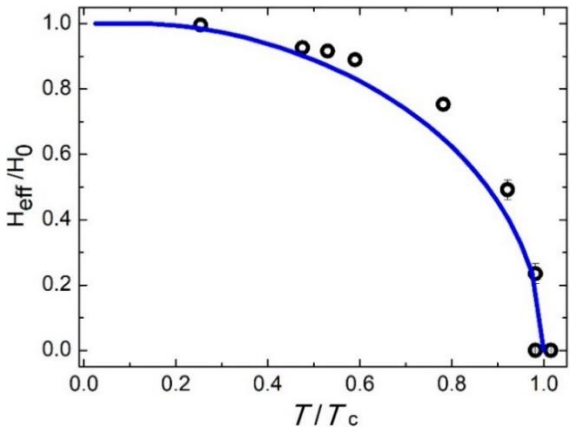

Figure 11. The temperature dependence (T_C = 390 K) of the magnetic hyperfine field in $MnFe_{0.5}Ru_{0.5}O_3$. The solid line represents a Brillouin function of S = 5/2.

Electrical Conductivity. The resistivity was measured on a pellet as a function of temperature between 5-300 K without applying a magnetic field (Figure 12)**.** Above 40 K, the resistivity decreases as the temperature increases, indicating semiconducting behavior. The high temperature data between 300 and 107 K can be linearly fitted with ln ϱ versus $1/T^{1/4}$, which agrees with the Mott's variable range hopping (VRH) conduction mechanism $\rho = \rho_0 \exp\left[\left(\frac{T_0}{T}\right)^{1/4}\right]$.[61] The fitting yields the parameters ρ_0 and T_0 equal to 4.14×10^{-9} Ω·cm and 2.03×10^6 K, respectively. The high temperature resistivity behavior and the fitting results are similar to those of $MnFe_{0.5}Ru_{0.5}O_3$, a FM VRH semiconductor.[29] The abnormal feature around 40 K may be related to the magnetic anomaly seen in Figure 7.

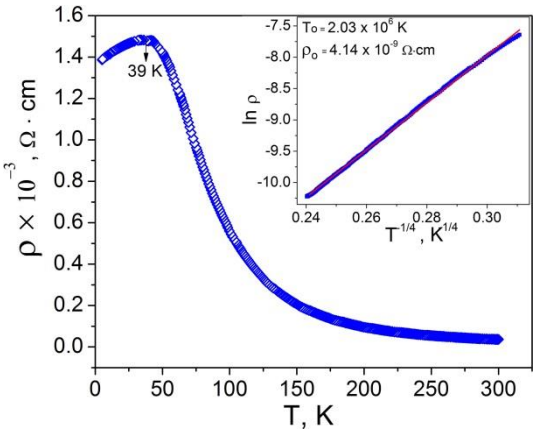

Figure 12. Resistivity (ϱ) as a function of temperature (T). The inset is the linear fit to the plot of ln ϱ versus $1/T^{1/4}$.

DFT calculations. Two possible crystal structures with α-Fe_2O_3 type, or LN-type were discussed in the diffraction analysis. To investigate which type of crystal structure is more stable energetically, DFT was utilized. The VCA method was employed to take into account the structural disorder. In the VCA

calculations, Ru disorder was assumed not to be critical to determine the stable crystal structure. Hence, Ru disorder was not considered and was simply replaced by Fe and only the Mn/Fe disorder was taken into account in the calculations. As a result, the crystal structure with α-Fe_2O_3 - type has lower energy than that with LN-type with an energy difference of 10.58 eV/atom. Therefore, even if Ru disorder would be considered in the VCA calculations, it would be unlikely to reverse the energy order, due to the significant energy difference, in agreement with experimental results.

Figure 13 shows the density of states for antiferromagnetic ordering in the α-Fe_2O_3 type crystal structure obtained from GGA + U calculations. The AFM order was adopted from Figure 9. The GGA + U calculation with AFM order clearly shows a band gap of 1.91 eV, which supports the semiconducting behavior observed in the experiments. The magnetic structure with α-Fe_2O_3-type possesses two symmetrically different Fe sites and the local moments of each Fe site are 4.06, - 4.07 μ_B/Fe, respectively. A weak ferromagnetic component with the magnitude of 0.004 μ_B/Fe is observed in the DFT calculation, which is consistent with the experiment. In Figure 13, the red broken line corresponds to the partial DOS for Fe-I 3d orbital. The partial DOS for Fe-I spin up is completely filled, because there is no DOS for Fe-I spin up above the Fermi level. Fe-II has the opposite occupancy. Therefore, both Fe-I and Fe-II show Fe^{3+} (d^5) with high spin configuration. In comparing the total energies of AFM and FM states in the GGA + U calculations, the AFM state has a lower energy by 0.098 eV/atom from that of the FM state.

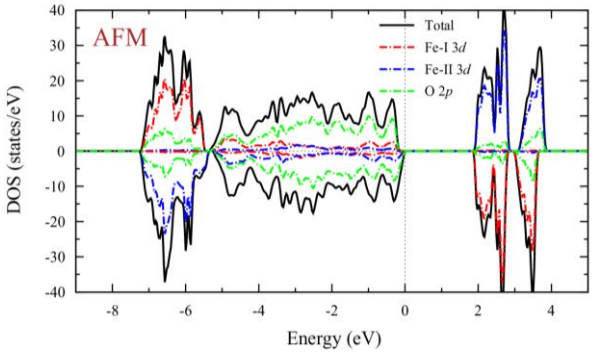

Figure 13. Density of states (DOS) in a-Fe_2O_3 type crystal structure with antiferromagnetism (AFM) obtained from GGA + U (= 4 eV) calculation. The magnetic structure possesses two symmetrically different Fe sites: Fe-I and Fe-II. Black line corresponds to the total DOS. Red, blue, and green lines represent Fe-I 3d , Fe-II 3d, and O 2p partial DOS, respectively. The positive and negative values in DOS correspond to spin up and down, respectively.

Comparison of $MnFe_{0.5}Ru_{0.5}O_3$ and Related $Mn_2BB'O_6$. To date, eight transition-metal-only $A_2BB'O_6$ (A = Mn, B = Fe, Mn, B' = Nb, Ta, W, Re) oxides have been successfully prepared under high pressure (5-8 GPa) and high temperature (1573–1875 K) (Table 3). While Mn_2MnReO_6 and Mn_2FeReO_6 form highly distorted DP (AO_8 with rock salt ordering of corner-linked BO_6 and $B'O_6$), other $A_2BB'O_6$ oxides form cation-ordered, noncentrosymmetric corundum derivatives, such as the LN and NTO phases (with face- and corner-linked six-coordinated AO_6, BO_6 and $B'O_6$ octahedra). In Mn_2FeNbO_6 and Mn_2FeTaO_6, the B and B' sites disorder due to the small size difference between Fe^{3+} and Nb^{5+} ions (0.005 Å), but the overall structure, with ordering of large Mn^{2+} ions on the A sites, is still polar LN-type which is stabilized by the second-order

Jahn-Teller effect of d^0 Nb^{5+}/Ta^{5+} ions. Mn_2FeWO_6 and Mn_2MnWO_6 crystallize in the NTO-type structure with ordered *B* and *B*' sites due to the large charge difference (4) and size difference (0.23 Å) between Fe^{2+} and W^{6+} ions. Although the charge difference (2) and size difference (0.035 Å) between Fe^{3+} and Mo^{5+} are small, Mn_2FeMoO_6 surprisingly also stabilizes in the NTO-type structure, which is attributed to FiM magnetic configuration that leads to the lowest energy state.

$MnFe_{0.5}Ru_{0.5}O_3$ is the first example of transition-metal-only $A_2BB'O_6$ phase that adopts the corundum structure with totally disordered *A*, *B*, and *B*' sites (Table 3). This lack of cation order is thought to arise due to the small size and charge difference between $Mn^{2+/3+}$, Fe^{3+} and $Ru^{3+/4+}$. The mixed-valence of $Mn^{2+/3+}$ and disorder in $MnFe_{0.5}Ru_{0.5}O_3$ is also likely related to the strong Jahn-Teller effect of $Mn^{3+}(3d^4)$, which is not favorable for face, or edge-sharing octahedra in corundum-related structures. The failure to oxidize Ru^{4+} to Ru^{5+} with MnO_2 during the synthesis causes $MnFe_{0.5}Ru_{0.5}O_3$ to stabilize in the non-polar corundum phase instead of DP, polar LN, or NTO phases. Ru^{5+} in this phase may be achieved by optimizing synthetic conditions e.g., with use of an oxidizing agent as $KClO_3$ or $KClO_4$, which converts to a KCl byproduct that can be easily washed away by water after the reaction.

The magnetic properties of $MnFe_{0.5}Ru_{0.5}O_3$ are different from those reported for $Mn_2FeB'O_6$. $Mn_2FeB'O_6$ (*B*' = Nb^{5+}, Ta^{5+}, W^{5+}) shows clear AFM ordering between 75-90 K, with weak FM~ 210 K for *B*' = Nb^{5+}, Ta^{5+} (Table 3) while Mn_2FeMoO_6 and Mn_2FeReO_6 exhibit FiM ordering above RT. The introduction of more d^n ($n > 0$) electrons at the *B*'-sites of $Mn_2FeB'O_6$ (B' = Mo^{5+}, Re^{5+}) changes the AFM to FiM ordering and also increases the ordering temperature dramatically. The ideal $Mn^{2+}{}_2Fe^{3+}Ru^{5+}O_6$ with an ordered polar structure is expected to show FM.

Table 3. Comparison of transition-metal-only $A_2BB'O_6$.

Compound	Synthesis	*A*, d^n, r[62]	*B*, d^n, r	*B*', d^n, r	Structure	T_C/T_N, K
Mn_2FeNbO_6[28]	MnO + Fe_2O_3 + Nb_2O_5, 1573 K, 7 GPa	Mn^{2+}, $3d^5$ 0.83 Å	Fe^{3+}, $3d^5$ 0.645 Å	Nb^{5+}, $4d^0$ 0.64 Å	LN, *R*3*c*	T_N = 90, T_C ~ 200,
Mn_2FeTaO_6[28]	MnO + Fe_2O_3 + Ta_2O_5, 1573 K, 7 GPa	Mn^{2+}, $3d^5$ 0.83 Å	Fe^{3+}, $3d^5$ 0.645 Å	Ta^{5+}, $5d^0$ 0.64 Å	LN, *R*3*c*	T_N = 80, T_C ~ 200
Mn_2FeWO_6[31]	MnO + Fe_2O_3 + Fe + WO_3, 1673 K, 8 GPa	Mn^{2+}, $3d^5$ 0.83 Å	Fe^{2+}, $3d^6$ 0.78Å	W^{6+}, $5d^0$ 0.60 Å	NTO, *R*3	T_N = 75
Mn_2FeMoO_6[29]	MnO + Fe_2O_3 + Fe + MoO_3, 1623 K, 8 GPa	Mn^{2+}, $3d^5$ 0.83 Å	Fe^{3+}, $3d^5$ 0.645 Å	Mo^{5+}, $4d^1$ 0.61 Å	NTO, *R*3	T_C = 337
$Mn_2(Fe_{0.8}Mo_{0.2})MoO_6$[63]	MnO + Fe_2O_3 + Fe + MoO_3 1623 K, 8 GPa	Mn^{2+}, $3d^5$ 0.83 Å	Fe^{3+}, $3d^5$ 0.645 Å	$Mo^{4/5+}$, $4d^{2/1}$ 0.65/0.61 Å	DP, $P2_1/n$	T_C = 194
Mn_2FeReO_6[30]	MnO + Fe_2O_3 + Fe + ReO_3,	Mn^{2+}, $3d^5$	Fe^{3+}, $3d^5$	Re^{5+}, $5d^2$	DP, $P2_1/n$	T_C = 520

	1873 K, 5 GPa	0.83 Å	0.645 Å	0.58 Å		
$MnFe_{0.5}Ru_{0.5}O_3$	$MnO + MnO_2 + Fe_2O_3 + RuO_2$, 1623 K, 5 GPa	$Mn^{2+/3+}$, $3d^{5/4}$ 0.83/0.645 Å	Fe^{3+}, $3d^5$ 0.645 Å	$Ru^{3/4+}$, $4d^{5/4}$ 0.562/0.62 Å	α-Fe_2O_3, $R\bar{3}c$	T_N ~ 400
Mn_2MnWO_6[60]	$MnO + WO_3$, 1673 K, 8 GPa	Mn^{2+}, $3d^5$ 0.83 Å	Mn^{2+}, $3d^5$ 0.83 Å	W^{6+}, $5d^1$ 0.60 Å	NTO, $R3$	T_N = 58
Mn_2MnReO_6[64]	$MnO + ReO_3$, 1673 K, 5 GPa	Mn^{2+}, $3d^5$ 0.83 Å	$Mn^{2+/3+}$, $3d^{5/4}$ 0.83/0.645 Å	$Re^{5+/6+}$, $5d^{2/1}$ 0.58/0.55 Å	DP, $P2_1/n$	T_N = 110

Conclusions

$MnFe_{0.5}Ru_{0.5}O_3$ is the first example of a cation-disordered corundum-derived oxide in the transition-metal-only $A_2BB'O_6$ series, which is synthesized by high pressure and high temperature. X-ray absorption K- and L- near edge spectroscopies establish mixed-valent $Mn^{2+/3+}$, Fe^{3+} and $Ru^{\sim 4+}$ formal oxidation states. The similar cation sizes and charges of metal ions provide a smaller driving force for ordering than in related systems containing small and highly charged B/B' ions along with a high content of the large A-site Mn^{2+} ion. This is reflected in the unit cell parameters and bond lengths, with a much smaller in-plane parameter (and unit cell volume) and shorter M – O bond lengths for $MnFe_{0.5}Ru_{0.5}O_3$ compared with ordered analogues such as $Mn_2FeB'O_6$ (B' = Nb^{5+}, Ta^{5+}, W^{6+}) and $Mn_2Mn^{2+}W^{6+}O6$, which all possess a much higher content of the large Mn^{2+} ion. This suggests that to design new cation-ordered corundum-derived materials, care must be taken to ensure the redox chemistry of the system to allow for a large A cation (such as Mn^{2+}, Zn^{2+}) with much smaller and more highly charged B/B' cations.

Analysis of the cation distribution in $MnFe_{0.5}Ru_{0.5}O_3$ highlights the importance of using several complementary structural characterization methods to confirm the symmetry and structure; neither XRPD nor NPD alone allowed the unambiguous determination of the disordered distribution of Mn, Fe and Ru ions. However, the similar X-ray scattering lengths of Mn and Fe, in contrast to the much heavier Ru combined with the very different neutron scattering lengths of Mn and Fe lead to the establishment of the cation-disordered $R\bar{3}c$ nuclear structure. This disordered model is consistent with transmission electron microscopy, XANES, and Mössbauer spectra results. The centrosymmetric nature is also confirmed by the absence of SHG signal.

NPD analysis confirms a collinear AFM magnetic structure (with moments in general direction) with T_N~400 K, which is in agreement with temperature-dependent magnetic and Mössbauer spectra results. The corundum structure and AFM ground state are supported by theoretical calculations. As a semiconductor with an ordering temperature above RT, $MnFe_{0.5}Ru_{0.5}O_3$ may be a potential candidate for spintronic applications.

Acknowledgements

M.G. thanks the NSF-DMR-1507252 grant of the United States. X.T., GK and CJK were supported by the "Center for Computational Design of Functional Strongly Correlated Materials and Theoretical Spectroscopy" under DOE Grant No. DE-FOA-0001276. MRCAT operations are supported by the Department of Energy and the MRCAT member institutions. EEM is grateful to the Leverhulme Trust (RPG-2017-362). M. R. Li and M. X. Wu are supported by the "One Thousand Youth Talents" Program of China. Use of the Advanced Photon Source at Argonne National Laboratory was supported by the U. S. Department of Energy, Office of Science, Office of Basic Energy Sciences, under Contract No. DE-AC02-06CH11357. Part of this research used the ISS, 8-ID and TES, 8-BM beamlines at the National Synchrotron Light Source II (NSLS-II), a U.S. Department of Energy (DOE) Office of Science User Facility operated for the DOE Office of Science by Brookhaven National Laboratory under Contract No. DE-SC0012704. Without the valuable aid/support of the NSLS-II staff scientists Eli Stavitski, Klaus Attenkofer, and Paul Northrup this phase of the work could not have been performed. The work at IOPCAS was supported by NSF & MOST of China through research projects. H.R. and V.G. acknowledge NSF-MRSEC Center for Nanoscale Science at Penn State through the grant number DMR-1820620. The authors would like to thank Ms. Jean Hanley at Lamont-Doherty Earth Observatory in Columbia University for making the high-pressure assemblies. The authors acknowledge the science and technology facility council (STFC) UK for the provision of neutron beam time. The authors would like to thank Daniel Nye for help on the Rigaku SmartLab X-ray diffractometer instrument in the Materials Characterization Laboratory at the ISIS Neutron and Muon Source.

Supporting Information

Rietveld refinement profiles of synchrotron and neutron data; TGA-DSC measurement; electron diffraction patterns; comparison of the Mn-K and Fe-K edge spectra for $MnFe_{0.5}Ru_{0.5}O_3$ and α-Fe_2O_3; evolution of the L3-edges of 4*d*-row transition metal compounds; ZFC-FC of $MnFe_{0.5}Ru_{0.5}O_3$ with different applied magnetic field; comparison of magnetic-only Bragg reflections; the intensity of magnetic reflections as a function of temperature: total reflection intensity; coercive field of $MnFe_{0.5}Ru_{0.5}O_3$ as a function of temperature; and illustration of AFM magnetic structure.

Present Address

[†](X. T.) Department of Chemistry and Biochemistry, George Mason University, Fairfax, VA, 22030, USA.

References

1. S. A. Wolf, D. D. Awschalom, R. A. Buhrman, J. M. Daughton, S. von Molnar, M. L. Roukes, A. Y. Chtchelkanova and D. M. Treger, *Science*, 2001, **294**, 1488-1495.

2. C. Chappert, A. Fert and F. N. Van Dau, *Nat. Mater.*, 2007, **6**, 813-823.

3. C. Felser, G. H. Fecher and B. Balke, *Angew. Chem., Int. Ed. Engl.*, 2007, **46**, 668-699.

4. A. P. Ramirez, R. J. Cava and J. Krajewski, *Nature*, 1997, **386**, 156-159.

5. W. Kobayashi, S. Ishiwata, I. Terasaki, M. Takano, I. Grigoraviciute, H. Yamauchi and M. Karppinen, *Phys. Rev. B: Condens. Matter Mater. Phys.*, 2005, **72**, 104408.

6. T. Katase, H. Takahashi, T. Tohei, Y. Suzuki, M. Yamanouchi, Y. Ikuhara, I. Terasaki and H. Ohta, *Adv. Electron. Mater.*, 2015, **1**, 1500199.

7. N. S. Rogado, J. Li, A. W. Sleight and M. A. Subramanian, *Adv. Mater.*, 2005, **17**, 2225-2227.

8. R. I. Dass, J. Q. Yan and J. B. Goodenough, *Phys. Rev. B: Condens. Matter Mater. Phys.*, 2003, **68,** 064415.

9. Y. Krockenberger, K. Mogare, M. Reehuis, M. Tovar, M. Jansen, G. Vaitheeswaran, V. Kanchana, F. Bultmark, A. Delin, F. Wilhelm, A. Rogalev, A. Winkler and L. Alff, *Phys. Rev. B: Condens. Matter Mater. Phys.*, 2007, **75**, 020404.

10. B. G. Park, J. Wunderlich, X. Marti, V. Holy, Y. Kurosaki, M. Yamada, H. Yamamoto, A. Nishide, J. Hayakawa, H. Takahashi, A. B. Shick and T. Jungwirth, *Nat. Mater.*, 2011, **10**, 347-351.

11. A. B. Shick, S. Khmelevskyi, O. N. Mryasov, J. Wunderlich and T. Jungwirth, *Phys. Rev. B: Condens. Matter Mater. Phys.*, 2010, **81**, 212409.

12. R. Duine, *Nat. Mater.*, 2011, **10**, 344-345.

13. T. Jungwirth, X. Marti, P. Wadley and J. Wunderlich, *Nat. Nanotechnol.*, 2016, **11**, 231-241.

14. C. Marrows, *Science*, 2016, **351**, 558-559.

15. P. Wadley, B. Howells, J. Zelezny, C. Andrews, V. Hills, R. P. Campion, V. Novak, K. Olejnik, F. Maccherozzi, S. S. Dhesi, S. Y. Martin, T. Wagner, J. Wunderlich, F. Freimuth, Y. Mokrousov, J. Kunes, J. S. Chauhan, M. J. Grzybowski, A. W. Rushforth, K. W. Edmonds, B. L. Gallagher and T. Jungwirth, *Science*, 2016, **351**, 587-590.

16. O. Gomonay, T. Jungwirth and J. Sinova, *Phys. Status Solidi Rapid Res. Lett.*, 2017, **11**, 1700022.

17. V. Baltz, A. Manchon, M. Tsoi, T. Moriyama, T. Ono and Y. Tserkovnyak, *Rev. Mod. Phys.*, 2018, **90**, 015005.

18. T. Jungwirth, J. Sinova, A. Manchon, X. Marti, J. Wunderlich and C. Felser, *Nat. Phys.*, 2018, **14**, 200-203.

19. P. Němec, M. Fiebig, T. Kampfrath and A. V. Kimel, *Nat. Phys.*, 2018, **14**, 229-241.

20. R. A. Duine, K.-J. Lee, S. S. P. Parkin and M. D. Stiles, *Nat. Phys.*, 2018, **14**, 217-219.

21. A. Beleanu, J. Kiss, G. Kreiner, C. Köhler, L. Müchler, W. Schnelle, U. Burkhardt, S. Chadov, S. Medvediev, D. Ebke, C. Felser, G. Cordier, B. Albert, A. Hoser, F. Bernardi, T. I. Larkin, D. Pröpper, A. V. Boris and B. Keimer, *Phys. Rev. B: Condens. Matter Mater. Phys.*, 2013, 88. 184429.

22. P. Wadley, V. Novak, R. P. Campion, C. Rinaldi, X. Marti, H. Reichlova, J. Zelezny, J. Gazquez, M. A. Roldan, M. Varela, D. Khalyavin, S. Langridge, D. Kriegner, F. Maca, J. Masek, R. Bertacco, V. Holy, A. W. Rushforth, K. W. Edmonds, B. L. Gallagher, C. T. Foxon, J. Wunderlich and T. Jungwirth, *Nat. Commun.*, 2013, **4**, 2322.

23. J. Mundelein and H. U. Schuster, *Z. Naturforsch. B*, 1992, **47**, 925-928.

24. X. Marti, I. Fina, C. Frontera, J. Liu, P. Wadley, Q. He, R. J. Paull, J. D. Clarkson, J. Kudrnovsky, I. Turek, J. Kunes, D. Yi, J. H. Chu, C. T. Nelson, L. You, E. Arenholz, S. Salahuddin, J. Fontcuberta, T. Jungwirth and R. Ramesh, *Nat. Mater.*, 2014, **13**, 367-374.

25. D. Kriegner, K. Vyborny, K. Olejnik, H. Reichlova, V. Novak, X. Marti, J. Gazquez, V. Saidl, P. Nemec, V. V. Volobuev, G. Springholz, V. Holy and T. Jungwirth, *Nat. Commun.*, 2016, **7**, 11623.

26. I. Fina, X. Marti, D. Yi, J. Liu, J. H. Chu, C. Rayan-Serrao, S. Suresha, A. B. Shick, J. Zelezny, T. Jungwirth, J. Fontcuberta and R. Ramesh, *Nat. Commun.*, 2014, **5**, 4671.

27. B. J. Kim, H. Ohsumi, T. Komesu, S. Sakai, T. Morita, H. Takagi and T. Arima, *Science*, 2009, **323**, 1329-1332.

28. M.-R. Li, D. Walker, M. Retuerto, T. Sarkar, J. Hadermann, P. W. Stephens, M. Croft, A. Ignatov, C. P. Grams, J. Hemberger, I. Nowik, P. S. Halasyamani, T. T. Tran, S. Mukherjee, T. S. Dasgupta and M. Greenblatt, *Angew. Chem., Int. Ed. Engl.*, 2013, **52**, 8406-8410.

29. M.-R. Li, M. Retuerto, D. Walker, T. Sarkar, P. W. Stephens, S. Mukherjee, T. S. Dasgupta, J. P. Hodges, M. Croft, C. P. Grams, J. Hemberger, J. Sanchez-Benitez, A. Huq, F. O. Saouma, J. I. Jang and M. Greenblatt, *Angew. Chem., Int. Ed. Engl.*, 2014, **53**, 10774-10778.

30. M.-R. Li, M. Retuerto, Z. Deng, P. W. Stephens, M. Croft, Q. Huang, H. Wu, X. Deng, G. Kotliar, J. Sanchez-Benitez, J. Hadermann, D. Walker and M. Greenblatt, *Angew. Chem., Int. Ed. Engl.*, 2015, **54**, 12069-12073.

31. M.-R. Li, M. Croft, P. W. Stephens, M. Ye, D. Vanderbilt, M. Retuerto, Z. Deng, C. P. Grams, J. Hemberger, J. Hadermann, W. M. Li, C. Q. Jin, F. O. Saouma, J. I. Jang, H. Akamatsu, V. Gopalan, D. Walker and M. Greenblatt, *Adv. Mater.*, 2015, **27**, 2177-2181.

32. L. C. Chapon, P. Manuel, P. G. Radaelli, C. Benson, L. Perrott, S. Ansell, N. J. Rhodes, D. Raspino, D. Duxbury, E. Spill and J. Norris, *Neutron News*, 2011, **22**, 22.

33. A. A. Coelho, *J. Appl. Cryst.*, 2003, **36**, 86.

34. A. A. Coelho, Topas Academic (5th edition), Bruker AXS, Karlsruhe, Germany, 2012.

35. B. J. Campbell, H. T. Stokes, D. E. Tanner and D. M. Hatch, *J. Appl. Cryst.*, 2006, **39**, 607-614.

36. C. Koch, PhD thesis, Arizona State University, 2002.

37. L. Bellaiche and D. Vanderbilt, *Phys. Rev. B: Condens. Matter Mater. Phys.*, 2000, **61**, 7877-7882.

38. P. Giannozzi, S. Baroni, N. Bonini, M. Calandra, R. Car, C. Cavazzoni, D. Ceresoli, G. L. Chiarotti, M. Cococcioni, I. Dabo, A. Dal Corso, S. de Gironcoli, S. Fabris, G. Fratesi, R. Gebauer, U. Gerstmann, C. Gougoussis, A. Kokalj, M. Lazzeri, L. Martin-Samos, N. Marzari, F. Mauri, R. Mazzarello, S. Paolini, A. Pasquarello, L. Paulatto, C. Sbraccia, S. Scandolo, G. Sclauzero, A. P. Seitsonen, A. Smogunov, P. Umari and R. M. Wentzcovitch, *J. Phys.: Condens. Matter*, 2009, **21**, 395502.

39. P. Giannozzi, O. Andreussi, T. Brumme, O. Bunau, M. B. Nardelli, M. Calandra, R. Car, C. Cavazzoni, D. Ceresoli, M. Cococcioni, N. Colonna, I. Carnimeo, A. Dal Corso, S. de Gironcoli, P. Delugas, R. A. DiStasio, A. Ferretti, A. Floris, G. Fratesi, G. Fugallo, R. Gebauer, U. Gerstmann, F. Giustino, T. Gorni, J. Jia, M. Kawamura, H. Y. Ko, A. Kokalj, E. Kucukbenli, M. Lazzeri, M. Marsili, N. Marzari, F. Mauri, N. L. Nguyen, H. V. Nguyen, A. Otero-de-la-Roza, L. Paulatto, S. Ponce, D. Rocca, R. Sabatini, B. Santra, M. Schlipf, A. P. Seitsonen, A. Smogunov, I. Timrov, T. Thonhauser, P. Umari, N. Vast, X. Wu and S. Baroni, *J. Phys.: Condens. Matter*, 2017, **29**. 465901.

40. D. Vanderbilt, *Phys. Rev. B: Condens. Matter Mater. Phys.*, 1990, **41**, 7892-7895.

41. P. S. Blaha, K.; Madsen, G. K. H.; Kavasnicka, D.; Luitz, J., *Schwarz, K., Ed.,* WIEN2k, *Technische Universität Wien: Wien, Austria*, 2001.

42. J. P. Perdew, K. Burke and M. Ernzerhof, *Phy. Rev. Lett.*, 1996, **77**, 3865-3868.

43. V. I. Anisimov, I. V. Solovyev, M. A. Korotin, M. T. Czyzyk and G. A. Sawatzky, *Phys. Rev. B: Condens. Matter Mater. Phys.*, 1993, **48**, 16929-16934.

44. A. VI, F. Aryasetiawan and A. I. Lichtenstein, *J. Phys. Condens. Matter*, 1997, **9**, 767-808.

45. G.-H. Cai, M. Greenblatt and M.-R. Li, *Chem. Mater.*, 2017, **29**, 5447-5457.

46. V. F. Sears, *Neutron News*, 1990, **3**, 29-37.

47. S. A. Denev, T. T. A. Lummen, E. Barnes, A. Kumar and V. Gopalan, *J. Am. Ceram. Soc*, 2011, **94**, 2699-2727.

48. F. M. F. de Groot, Z. W. Hu, M. F. Lopez, G. Kaindl, F. Guillot and M. Tronc, *J. Chem. Phys.*, 1994, **101**, 6570-6576.

49. K. V. Ramanujachary, S. E. Lofland, W. H. McCarroll, T. J. Emge, M. Greenblatt and M. Croft, *J. Solid State Chem.*, 2002, **164**, 60-70.

50. F. d. Groot, *Coord. Chem. Rev.*, 2005, **249**, 31-63.

51. G. M. Veith, M. Greenblatt, M. Croft, K. V. Ramanujachary, J. Hattrick-Simpers, S. E. Lofland and I. Nowik, *Chem. Mater.*, 2005, **17**, 2562-2567.

52. R. O. Bune, M. V. Lobanov, G. Popov, M. Greenblatt, C. E. Botez, P. W. Stephens, M. Croft, J. Hadermann and G. Van Tendeloo, *Chem. Mater.*, 2006, **18**, 2611-2617.

53. M. Retuerto, M.-R. Li,, Y. B. Go, A. Ignatov, M. Croft, K. V. Ramanujachary, J. Hadermann, J. P. Hodges, R. H. Herber, I. Nowik and M. Greenblatt, *Inorg. Chem.*, 2012, **51**, 12273-12280.

54. Z. Hu, H. von Lips, M. S. Golden, J. Fink, G. Kaindl, F. M. F. de Groot, S. Ebbinghaus and A. Reller, *Phys. Rev. B: Condens. Matter Mater. Phys.*, 2000, **61**, 5262-5266.

55. R. Nepal, Q. Zhang, S. Dai, W. Tian, S. E. Nagler and R. Jin, *Phys. Rev. B: Condens. Matter Mater. Phys.*, 2018, **97**, 024410.

56. M. C. Kemei, J. K. Harada, R. Seshadri and M. R. Suchumel, *Phys. Rev. B: Condens. Matter Mater. Phys.*, 2014, **90**, 064418.

57. A. J. Dos santos-García, E. Solana-Madruga, C. Ritter, A. Andrada-Chacón, J. Sánchez-Benítez, F. J. Mompean, M. Garcia-Hernandez, R. Sáez-Puche and R. Schmidt, *Angew. Chem.; Int. Ed. Engl.*, 2017, **56**, 4438-4442.

58. I. Zivkovic, K. Prsa, O. Zaharko and H. Berger, *J. Phys. Condens. Matter*, 2010, **22**, 056002.

59. Y. S. Oh, S. Artyukhin, J. J. Yang, V. Zapf, J. W. Kim, D. Vanderbilt and S. W. Cheong, *Nat. Commun.*, 2014, **5**, 3201.

60. M.-R. Li, E. E. McCabe, P. W. Stephens, M. Croft, L. Collins, S. V. Kalinin, Z. Deng, M. Retuerto, A. Sen Gupta, H. Padmanabhan, V. Gopalan, C. P. Grams, J. Hemberger, F. Orlandi, P. Manuel, W. M. Li, C. Q. Jin, D. Walker and M. Greenblatt, *Nat. Commun.*, 2017, **8**, 2037.

61. N. F. Mott, *Conduction in Non-Crystalline Materials,* 2nd ed. Clarendon Press, Oxford. 1993.

62. R. D. Shannon, *Acta Cryst.*, 1976, **A32**, 751.

63. M.-R. Li, P. W. Stephens, M. Croft, Z. Deng, W. Li, C. Jin, M. Retuerto, J. P. Hodges, C. E. Frank, M. Wu, D. Walker and M. Greenblatt, *Chem. Mater.*, 2018, **30**, 4508-4514.

64. M.-R. Li, J. P. Hodges, M. Retuerto, Z. Deng, P. W. Stephens, M. C. Croft, X. Deng, G. Kotliar, J. Sánchez-Benítez, D. Walker and M. Greenblatt, *Chem. Mater.*, 2016, **28**, 3148-3158.

Table of Contents Graphic

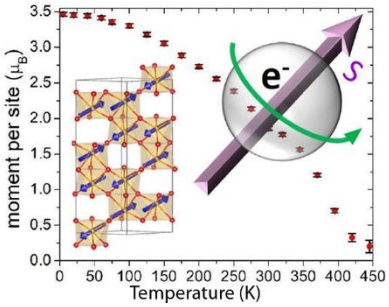

$MnFe_{0.5}Ru_{0.5}O_3$ is discovered at high pressure high temperature as an above-room-temperature antiferromagnetic semiconductor for potential spintronic application.